

Generation of Intense Low-Divergence Isolated Soft-X-Ray Attosecond Pulses in a Gas-Filled Waveguide Using Three-Color Synthesized Laser Pulses

Baochang Li,¹ Xiangyu Tang,¹ Kan Wang,¹ Chi Zhang¹, Zhong Guan,¹ Bincheng Wang,¹ C. D. Lin², and Cheng Jin^{1,3*}

¹*Department of Applied Physics, Nanjing University of Science and Technology, Nanjing, Jiangsu 210094, China*

²*J. R. Macdonald Laboratory, Department of Physics, Kansas State University, Manhattan, Kansas 66506, USA*

³*MIIT Key Laboratory of Semiconductor Microstructure and Quantum Sensing, Nanjing University of Science and Technology, Nanjing, Jiangsu 210094, China*

(Received 23 May 2022; revised 8 August 2022; accepted 16 August 2022; published 19 September 2022)

Isolated attosecond pulses (IAPs) in the soft-x-ray (SXR) region have been successfully produced via high-order harmonic generation in a gas medium at several laboratories, but pulse energies are much lower compared to the IAPs in the extreme ultraviolet. Here, we show that in a gas-filled hollow waveguide, an efficient gating method using a few-cycle three-color synthesizer is able to generate stronger SXR IAPs. We show that an 104-as IAP in the SXR region (central energy of 210 eV) with a higher pulse energy (0.9 nJ) and a lower divergence (within 1.5 mrad) can be generated with a three-color laser beam for input pulse energy at 0.62 mJ, under the condition of optimal gas pressure and waveguide length. The enhancement of the IAP is attributed to favorable phase matching of SXR high harmonics caused by the evolution of the three-color waveform during its propagation in the waveguide, which can be understood by analyzing the time shift of the waveform due to the interplay of the waveguide mode, atomic dispersion, and plasma dispersion. We check that the gating method is quite robust with respect to the phase jitter in the waveform. The advantage of this method is further demonstrated by comparing the generation of SXR high harmonics and attosecond pulses with two other schemes: the three-color waveform in a gas cell and a previously optimized two-color waveform in a gas-filled waveguide.

DOI: 10.1103/PhysRevApplied.18.034048

I. INTRODUCTION

In recent years, high-order harmonic generation (HHG) due to the interaction between an intense femtosecond laser pulse and an atomic gas medium has been developed to an effective way to produce table-top isolated attosecond light sources [1]. These attosecond pulses enable us to capture the motion of electrons in atomic, molecular, and solid materials [2–5]. Since the report of the first isolated attosecond pulse (IAP) in 2001 [6], attosecond science has progressed continuously. One of the major efforts in this field is to produce reliable short, bright IAPs in the spectral region from the extreme ultraviolet (XUV) to soft x rays.

In the past two decades, several methods have been established to produce IAP in the XUV, and they can be generally divided into two categories. One is to control the waveform of the driving laser to limit harmonic emission to occur only over a short period, such as amplitude gating [6–8], polarization gating [9,10], double-optical gating [11–15], and multicolor waveform synthesis [16–18].

The other is to regulate the phase matching of HHG during its propagation in the macroscopic medium where only a few parts of the harmonic emission can be coherently built up, like ionization gating [19], phase matching in the overdriven regime [20,21], attosecond lighthouse [22], and transient phase-matching gating [23–25]. So far, the XUV IAPs can reach energy at the μJ level. For example, Takahashi *et al.* [17] reported an IAP with 500-as pulse duration and 1.3- μJ pulse energy in the XUV regime (central energy at 30 eV), generated by two-color field synthesis. Xue *et al.* [26] applied a stable 50-mJ three-channel optical waveform synthesizer to generate continuum XUV spectrum (50 to 70 eV), and the corresponding pulse energy was 0.24 μJ , supporting an isolated 226-as IAP from their recent attosecond streaking measurement [27].

With the advance of midinfrared (MIR) laser technology, soft-x-ray (SXR) IAP (> 100 eV) has been produced since 2010 [23,28]. However, the pulse energy is much lower than that of the XUV IAP, as shown in the few experiments in which the SXR IAPs have been characterized. In Li *et al.* [29], the flux of a 53-as IAP with central energy of 170 eV was estimated to be 5×10^6 photons per laser shot, which corresponds to the pulse energy of

*Corresponding author. cjin@njust.edu.cn

about 100 pJ. They later reported a 302-as IAP with pulse energy of 300 pJ in the spectral region of 100–250 eV [30]. Cousin *et al.* [31] claimed a 322-as pulse with photon energy up to 350 eV, with pulse energy of about 0.3 pJ. In other examples where SXR harmonic spectra were generated using MIR lasers but their temporal waveforms were not characterized, the pulse energies in general are also lower. Teichmann *et al.* [32] used a carrier-envelope-phase- (CEP) stabilized few-cycle pulse at wavelength of 1.85 μm to interact with Ne, to obtain photon flux of $(2.8 \pm 0.1) \times 10^7$ photons/s per 10% bandwidth at 248 eV, corresponding to 2.9 ± 0.1 pJ. Johnson *et al.* [33] obtained high harmonics in the water-window spectral region with the maximum flux of 4×10^7 photons/s (corresponding to the pulse energy of 2 pJ). Recently, Takahashi's group [34,35] injected a 1.55- μm laser with loose focusing geometry into a long gas cell filled with high-pressure helium gas, the energy of resulting water-window harmonics was 3.53 nJ. All of these SXR IAPs are still much weaker than the mJ-level XUV IAPs. Therefore, it is highly desirable to find more efficient gating methods to increase the pulse energy of IAP in the SXR region.

In recent years, another effort for the generation of HHG light source is to obtain low divergence harmonic beam without the need of additional focusing optics [36]. The possible solutions include the use of a spatially chirped beam [37] or a two-color orthogonally polarized laser pulse [38]. Very recently, Rego *et al.* [39] tuned the divergence property of the XUV and SXR high-harmonic combs with an optimally phased necklace laser beam formed by different orbital-angular-momentum modes, resulting in HHG emission on the axis with extremely low divergence. Meanwhile, SXR harmonics generated with the MIR laser showed large angular divergence [40,41]. Thus, it is critical to generate SXR IAPs with low divergence as well. Preferably, it is desirable that both the issues of enhancing harmonic yields and reducing beam divergence of the IAP in the SXR region can be achieved by discovering a gating method.

To increase the conversion efficiency of IAP in the SXR region, one can modify subcycle laser waveform [42–45]. This technology is mature today due to the advance in optical parametric amplification (OPA) and optical parametric chirped pulse amplification (OPCPA). Any optical waveform in principle can be generated by accurately controlling the synthesis of multicolor laser pulses [17,26,43,46–51]. From the theoretical side, we have previously proposed two- and three-color waveforms to enhance single-atom SXR harmonic yields through enhancing “short”-trajectory harmonic emissions [52], where it is possible to limit the total ionization around a “critical” level [53]. Such waveforms are expected to generate bright high harmonics since the harmonics can be easily phase matched in the gas medium to obtain high intensity and can be emitted with low divergence in the far field. To achieve such a goal one needs to adopt the proper generation equipment and to fine tune the macroscopic conditions. Meanwhile, one also needs to determine which waveform can be utilized to ensure the efficient gating of the IAP. In this work, we choose a three-color waveform by optimally synthesizing a sinusoidal fundamental laser pulse with its second and fourth harmonic fields as the driving laser, and choose a hollow waveguide filled with gas medium as HHG generation setup. The waveguide device is a commonly used apparatus for generating high-order harmonics, especially for creating quasi-phase-matching conditions [54–57]. By propagating light pulse through a waveguide, its phase velocity can be carefully controlled and the effect of beam divergence can be eliminated, so a geometry of the near plane wave can be realized [53,58]. In addition, the pressure of gas medium can be accurately controlled through the waveguide device in HHG experiments [59–61].

The main goal of this paper is to establish an effective gating method by using a three-color synthesized waveform in a hollow waveguide filled with neon gas to generate intense and low-divergent IAP in the SXR region. As shown in Fig. 1, the three-color optimized waveform consists of midinfrared (1600 nm), near-infrared (800 nm),

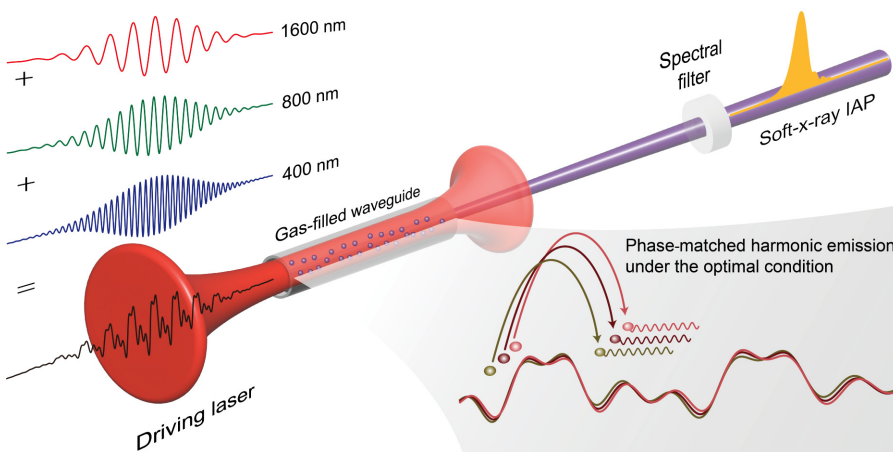


FIG. 1. Schematic of a three-color Gaussian beam guiding into a gas-filled waveguide and the generation of soft-x-ray IAP by spectrally filtering of phase-matched high harmonics.

and ultraviolet (400 nm) laser pulses. Combining with such a powerful waveguide, the propagation of such a waveform and phase matching of the resulting SXR high harmonics can be optimized by adjusting macroscopic conditions. At the optimal condition of gas pressure of 70 Torr and waveguide length of 5 mm, we find that conversion efficiency of 10^{-6} can be achieved for the continuous SXR high harmonics from 140 to 280 eV, and the pulse energy of the synthesized IAP is 0.9 nJ. Meanwhile, we show that the pulse duration of the IAP is 104 as, without any additional phase compensation by any filters, and the resulting divergence in the far field is less than 1.5 mrad. We examine the time-frequency harmonic emission and the driving three-color laser waveform at the intermediate propagation steps in the waveguide, and uncover the phase-matching mechanism of HHG by calculating the variation of single-atom intrinsic phase. The robustness of this IAP generation scheme will be checked by introducing jitters for the relative phase in the three-color waveform. We further show the generation of SXR high harmonics and IAP by using the same three-color waveform but in a gas cell, and a different phase-matching mechanism is discussed. Finally, we give HHG spectra and attosecond pulses in the SXR region by using a previously optimized two-color waveform in the gas-filled waveguide.

II. THEORETICAL METHODS

A. Propagation equations in a gas-filled waveguide

To simulate SXR high harmonics generated in a gas-filled waveguide by using a three-color synthesized waveform, one needs to calculate both single-atom response and macroscopic response. We employ the quantitative rescattering (QRS) model [62] to calculate the single-atom response, which is an improvement of the strong-field approximation [63]. The accuracy of the QRS model with multicolor laser pulses has been calibrated against the results of solving three-dimensional time-dependent Schrödinger equation in Ref. [64]. The macroscopic response is calculated by solving the propagation equations of the driving laser beam and the high-harmonic field in the nonlinear gas medium. Here, we discuss only how to formulate and solve these equations in a hollow waveguide. Details of these equations in a gas cell or gas jet have been given in Refs. [65–67].

In the time domain and in the rest frame, Maxwell's wave equation (MWE) for the driving laser pulse can be expressed in cylindrical coordinates as [65–67]

$$\nabla^2 E_1(r, z, t) - \frac{1}{c^2} \frac{\partial^2 E_1(r, z, t)}{\partial t^2} = \mu_0 \frac{\partial J_{\text{abs}}(r, z, t)}{\partial t} + \frac{\omega_0^2}{c^2} (1 - n_{\text{eff}}^2) E_1(r, z, t), \quad (1)$$

where $E_1(r, z, t)$ and ω_0 are the transverse electric field and angular frequency of the fundamental driving laser, respectively. n_{eff} represents the effective refractive index of the nonlinear gas medium, including the refraction effects of the neutral atoms, the optical Kerr nonlinearity, and the plasma. $J_{\text{abs}}(t)$ is the absorption term due to ionization.

Similarly, the MWE of the SXR high-harmonic field can be written as

$$\nabla^2 E_h(r, z, t) - \frac{1}{c^2} \frac{\partial^2 E_h(r, z, t)}{\partial t^2} = \mu_0 \frac{\partial^2 P(r, z, t)}{\partial t^2}, \quad (2)$$

where $E_h(r, z, t)$ is the electric field of the high-harmonic field. The polarization $P(r, z, t)$ consists of both linear and nonlinear parts. The latter term is related to the single-atom induced dipole moment $D(r, z, t)$.

Equations (1) and (2) can be rewritten in a reference frame ($z' = z$ and $t' = t - z/c$) moving at the speed of light c . The equation is then transformed to the frequency domain and solved using the split-operator method. For example, the propagation of the driving laser field in Eq. (1) from the plane (r, z) to $(r, z + \Delta z)$ can be obtained by solving two differential equations:

$$i \frac{2\omega}{c} \frac{\partial E_1(r, z', \omega)}{\partial z'} = \nabla_\perp^2 E_1(r, z', \omega), \quad (3)$$

and

$$\begin{aligned} & -i \frac{2\omega}{c} \frac{\partial E_1(r, z', \omega)}{\partial z'} \\ &= \hat{F} \left\{ \mu_0 \frac{\partial J_{\text{abs}}(r, z', t')}{\partial t'} + \frac{\omega_p^2}{c^2} E_1(r, z', t') \right. \\ & \quad \left. - 2 \frac{\omega_0^2}{c^2} [\delta_1 + n_2 I(r, z', t')] E_1(r, z', t') \right\}. \end{aligned} \quad (4)$$

Here δ_1 is refraction index, n_2 is the optical Kerr coefficient, ω_p is the plasma frequency, and \hat{F} is the Fourier transform operator.

The driving laser field propagating inside the hollow waveguide can be expanded by using waveguide eigenmodes as [68]

$$E_1(r, z', \omega) = \sum_m b_m(\omega, z') J_0 \left(\mu_m \frac{r}{a} \right), \quad (5)$$

where b_m is the complex expansion coefficient, μ_m is the m th root of the Bessel function of the first kind, i.e., $J_0(\mu_m) = 0$, and a is the waveguide radius. Inserting Eq. (5) into Eq. (3), and using the orthogonal relation of the Bessel function, we obtain the complex expansion

coefficient [69]:

$$b_m(\omega, z' + \Delta z') = b_m(\omega, z') \exp \left\{ \left[\frac{i\lambda}{4\pi} \left(\frac{\mu_m}{a} \right)^2 - \left(\frac{\mu_m}{2\pi} \right)^2 \frac{\lambda^2}{a^3} \frac{n_r^2 + 1}{2\sqrt{n_r^2 - 1}} \right] \Delta z' \right\}. \quad (6)$$

Here λ is the wavelength and n_r is the refractive index of the waveguide cladding, and the complex coefficient b_m is further modified by solving Eq. (4).

Note that the SXR high-harmonic field in Eq. (2) can be solved in a similar manner. In the simulation, we assume that the incident three-color Gaussian beams are focused on the entrance plane of the hollow waveguide. When the ratio of the beam waist of each color to the radius of the waveguide is set as 0.64, the spatial distribution of the three-color laser pulse at the entrance is known to be very close to the lowest EH₁₁ mode [70], where its transverse amplitude is very close to the Gaussian beam at the focus.

B. Far-field harmonic emission

High harmonics calculated at the exit of the gas medium are called near-field harmonics, and those collected by the spectrometer are called far-field harmonics. The far-field harmonic E_h^f at position z_f can be calculated from the near-field one through Hankel transformation:

$$\begin{aligned} E_h^f(r_f, z_f, \omega) &= -ik \exp \left[ik \left(\sqrt{z_f^2 + r_f^2} - z_f \right) \right] \\ &\times \int \frac{E_h(r, z', \omega)}{z_f - z'} J_0 \left(\frac{krr_f}{z_f - z'} \right) \\ &\times \exp \left[\frac{ik \left(r^2 + r_f^2 \right)}{2(z_f - z')} \right] r dr, \end{aligned} \quad (7)$$

where r_f is the radial distance on the far-field plane, J_0 is the zero-order Bessel function, $k = \omega/c$ is the wave vector, and z' is the near-field position.

C. Time-frequency analysis and generation of attosecond pulses

To analyze the harmonic emission in time, we use time-frequency picture based on the wavelet transform in the following [71,72]:

$$A(t, \omega) = \int E_h(\tau) w_{t,\omega}(\tau) d\tau, \quad (8)$$

with the wavelet kernel $w_{t,\omega}(\tau) = \sqrt{\omega} W[\omega(\tau - t)]$. The Morlet wavelet is chosen as [72]

$$W(x) = (1/\sqrt{\nu}) e^{ix} e^{-x^2/2\nu^2}. \quad (9)$$

Here ν is a constant. In our simulations, this value is 12 for best resolution.

To synthesize attosecond pulse, a range of harmonics (ω_1 – ω_2) are selected by applying a spectral filter. Total intensity of attosecond pulses in the near field is calculated as [66]

$$I_{\text{near}}(t) = \int_0^\infty 2\pi r dr \left| \int_{\omega_1}^{\omega_2} E_h(r, \omega) e^{i\omega t} d\omega \right|^2. \quad (10)$$

In the far field, we use a spatial filter to select harmonic emission within 1.5 mrad, which is circular with a radius of r_d . Intensity of attosecond pulses in the far field is

$$I_{\text{far}}(t) = \int_0^{r_d} 2\pi r_f dr_f \left| \int_{\omega_1}^{\omega_2} E_h^f(r_f, \omega) e^{i\omega t} d\omega \right|^2. \quad (11)$$

III. OPTIMAL GENERATION OF HHG AND IAP BY A THREE-COLOR WAVEFORM IN A GAS-FILLED HOLLOW WAVEGUIDE

A. Three-color optimized laser waveform

In the simulations, we adopt a three-color optimized waveform obtained in Ref. [52] as the driving laser field. This waveform is able to maximize single-atom HHG yields with cutoff energy of 250 eV in the SXR region and to enhance harmonic emissions from “short” electron trajectories while the resulted ionization level can be maintained to within 2%. It is expected that low-divergence SXR harmonics can be obtained in the far field if these “short”-trajectory harmonic emissions can be built up after the macroscopic propagation. The electric field of the three-color waveform is written as

$$\begin{aligned} E(t) &= E_1 A_1(t) \cos(\omega_1 t + \phi_1) + E_2 A_2(t) \cos(\omega_2 t + \phi_2) \\ &+ E_3 A_3(t) \cos(\omega_3 t + \phi_3). \end{aligned} \quad (12)$$

Here E_i , A_i , ω_i , and ϕ_i ($i = 1, 2, 3$) are field amplitude, temporal envelope function, angular frequency, and CEP for each wavelength component, respectively. These laser parameters are listed in Table I. We assume that each $A_i(t)$ has a Gaussian temporal envelope and each is represented by its duration of FWHM.

TABLE I. Laser parameters of the optimized three-color waveform [52].

λ_i	$ E_i ^2$	ϕ_i	FWHM
1.6 μm	2.03 I_0^a	0 π	3 OC ^b
0.8 μm	1.00 I_0	0.27 π	3 OC
0.4 μm	0.57 I_0	1.49 π	3 OC

^a $I_0 = 10^{14} \text{ W/cm}^2$

^bOC is defined with respect to wavelength of 1.6 μm

B. Generation of HHG and IAP in the SXR region under optimal macroscopic condition

In simulating macroscopic high harmonics in the SXR region, we consider that the neon gas is uniformly distributed inside the hollow waveguide. For each color, the spatial distribution of each laser beam is assumed to be Gaussian. The radius of the hollow waveguide is fixed at 125 μm . The beam waist of the incident Gaussian beam is chosen to be 80 μm to ensure that only the fundamental mode is present at the beginning of the waveguide. The input pulse energy is 0.62 mJ. Gas pressure and waveguide length are variables in the simulations.

We first plot the spectra of the total harmonic yields at the exit of waveguide generated by the optimized three-color waveform in Fig. 2(a). The length of waveguide is optimized at 5 mm, and the gas pressure is varied to achieve the highest harmonic yields in the whole spectral range. At a very low gas pressure of 5 Torr, the cutoff energy after macroscopic propagation is lower than the

cutoff energy from the single atoms. As it is well known that once the propagation is considered, it would introduce a geometric phase from the focused laser beam or from the waveguide mode. If such a phase is not canceled out by the phase of single-atom-induced dipole, there will be no phase matching such that even at 5 Torr, the cutoff energy will be modified. At a higher pressure (70 Torr in the present example), additional pressure-dependent phase-matching terms can be added to reach good phase matching. By increasing the gas pressure, the harmonic yield increases rapidly and reaches maximum at 70 Torr. One can see the HHG cutoff at 250 eV, in agreement with that obtained in the single-atom response. If the gas pressure is further increased, the harmonic yield decreases over the whole spectral region. In Fig. 2(a), we also show the harmonic spectrum generated by a single-color (1.6- μm) laser with peak intensity of $3.0 \times 10^{14} \text{ W/cm}^2$ at gas pressure of 70 Torr for comparison while other macroscopic parameters are the same. For SXR high harmonics in the

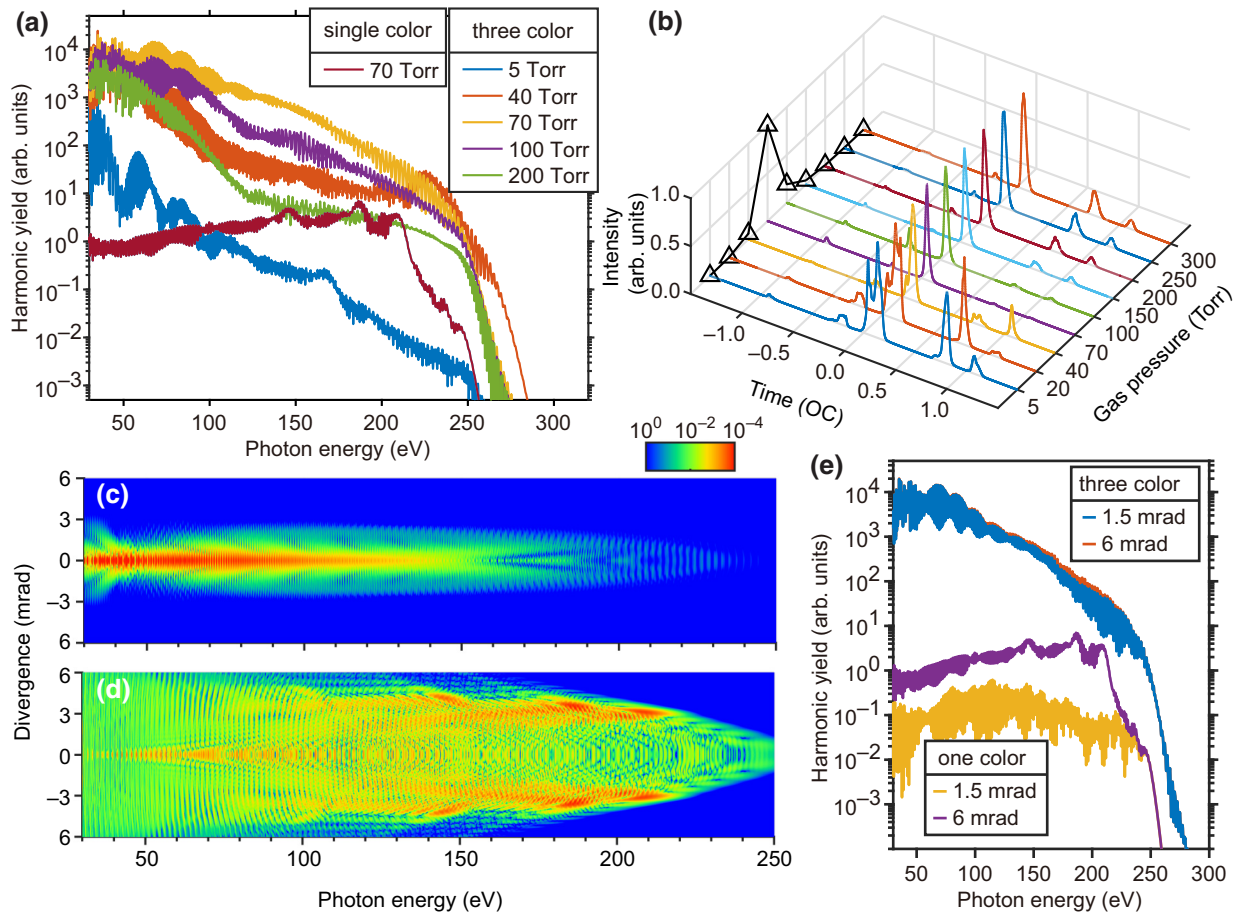


FIG. 2. (a) Macroscopic high-harmonic spectra at different gas pressures by the three-color waveform, and (b) attosecond pulse obtained by synthesizing high harmonics from 140 to 280 eV. For comparison, HHG spectrum at 70 Torr by the single-color laser is also plotted in (a). Optical cycle (OC) is defined with respect to the 1.6- μm laser. (c),(d) Harmonic intensity distributions in the far field for three-color and single-color waveforms at 70 Torr, respectively. (e) Plots of the HHG spectra by integrating far-field intensities within 1.5 and 6 mrad, respectively. See text for other laser and waveguide parameters.

region of 140 to 280 eV, the optimal conversion efficiency by the three-color waveform is 10^{-6} , which is 2 orders of magnitude higher than that by the single-color waveform.

We next select SXR harmonics from 140 to 280 eV (with central energy of 210 eV) in the near field to synthesize attosecond pulses. The temporal intensity (normalized) profiles and their pulse energies (black triangles) versus gas pressure are shown in Fig. 2(b). In a three-color waveform, the addition of the second and fourth harmonics to the fundamental pulse destroys the half-cycle periodicity such that harmonic emission occurs only once in each optical cycle of the fundamental. Considering the laser pulse duration of three optical cycles (OCs) with respect to the fundamental wavelength of $1.6 \mu\text{m}$, the synthesized attosecond pulse in the same spectral region has two main peaks, around 0 OC and 0.75 OC, respectively (also see Fig. 3). Figure 2(b) shows that isolated attosecond pulse shows up when gas pressure is varied from 40 to 150 Torr, and the optimal one with the highest pulse energy is at 70 Torr. This indicates that the generation of IAP is not only due to the three-color waveform but also enhanced by phase matching as the high harmonics propagate in the waveguide. We will carefully analyze this latter effect in Sec. III C.

We next compare the intensity profile of HHG in the far field using the three-color pulse with the single-color

pulse, in Figs. 2(c) and 2(d). In both cases, the gas pressure is at 70 Torr, and the harmonic intensity is normalized with the respective maximum value in each case. One can see that harmonic emissions are mainly localized along the propagation axis for the three-color case, while for the single-color case, the harmonics are distributed mostly off the axis, i.e., with large divergence. In Fig. 2(e), the total far-field harmonics yields integrated over 1.5 and over 6 mrad are compared, for the optimized three-color waveform and for the single-color one. This again demonstrates that the optimized three-color waveform can generate a much more intense SXR IAP but also has the desired property that the generated IAP would have a small divergence such that “refocusing” the SXR beam as an attosecond light source is not needed.

C. Analysis of the phase-matching mechanism of IAP generation

Here we analyze how the three-color waveform is modified in the generation of the IAP during its propagation in the hollow waveguide. We take two examples of APT generation at 5 Torr and IAP generation at the optimal pressure of 70 Torr for investigation. Intensities of time-frequency emissions of the harmonic field $E_h(r, z', t)$ at an off-axis radial position of $r = 42 \mu\text{m}$ are plotted in

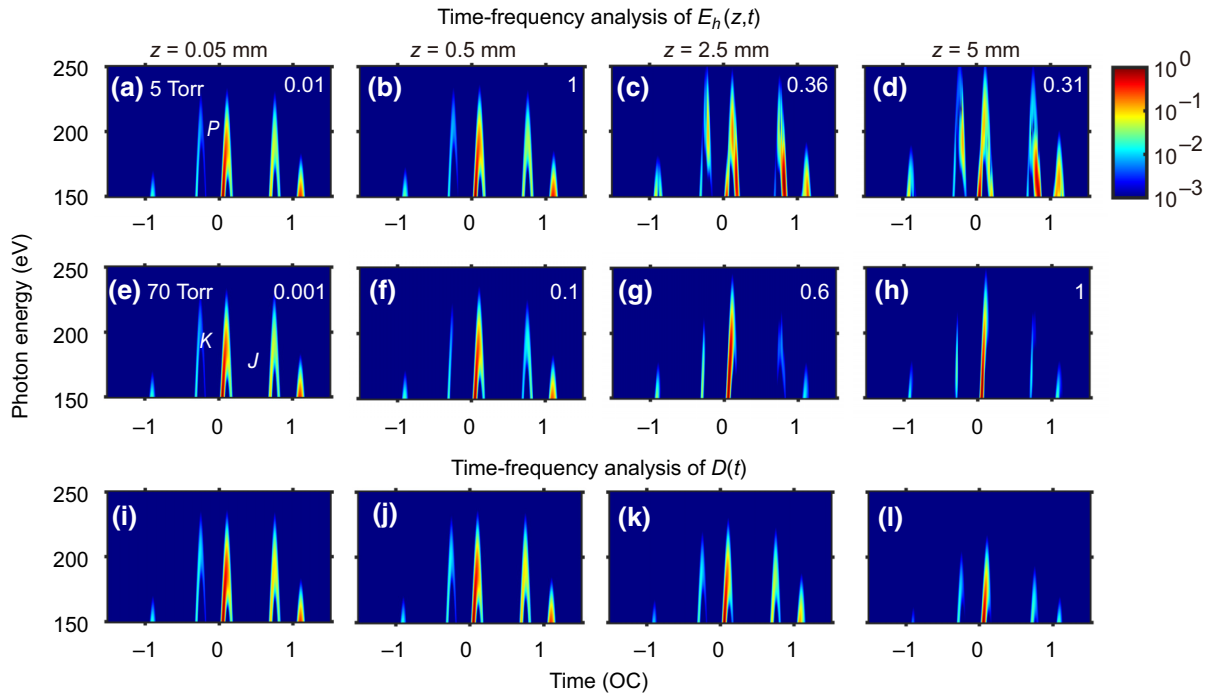


FIG. 3. (a)–(h) Time-frequency analysis of the harmonic field $E_h(z, t)$ accumulated from the entrance to the exit of the waveguide. First row, 5 Torr; second row, 70 Torr. Normalization factor for harmonic intensity is labeled on the top right in each figure. Along the same row, the change of harmonic intensity with propagation distance is indicated by comparing of normalization factors. (i)–(l) Time-frequency picture of single-atom-induced dipole moment $D(t)$ caused by the three-color electric field at different propagation distance for gas pressure of 70 Torr. The radial position is fixed at $r = 42 \mu\text{m}$.

Figs. 3(a)–3(h) for four selected propagation distances. Note that an off-axis radial position is chosen as a representative for analysis. And we have checked that near-field harmonic emissions at this position contribute considerably to the far-field harmonic according to Eq. (7). For 5 Torr, for instance, the harmonic emission labeled as “P” in Fig. 3(a) is first enhanced from $z = 0.05$ to 0.5 mm, and then is decreased from $z = 0.5$ to 5 mm. This can be seen clearly from the normalization factors in Figs. 3(a)–3(d). For 70 Torr, at a very short distance of $z = 0.05$ mm (near the entrance), in Fig. 3(e), there are two strong emission bursts around 0 and 0.75 OC, which are labeled by “K” and “J,” respectively. With the increase of propagation distance, the emission burst “K” remains strong while the emission burst “J” is weakened, as shown in Figs. 3(f) and 3(g). At the exit of waveguide (i.e., $z = 5$ mm), the emission burst “K” stands out as an isolated burst, as seen in Fig. 3(h), and it has a positive attochirp to preserve the characteristic “short”-trajectory harmonic emissions, thus leading to low-divergence high harmonics in the far field. Can the emission bursts “K” and “J” solely be caused by the modification of the three-color waveform during the propagation? To verify it, we show time-frequency plots of single-atom-induced dipoles caused by the propagated waveforms, in Figs. 3(i)–3(l). These pictures show that the emission bursts “J” from single-atom emitters are always considerable, however, due to phase mismatch, the field strength cannot be accumulated upon propagation.

We further plot the off-axis ($r = 42 \mu\text{m}$) electric fields of the three-color waveform at the entrance, the middle,

and the exit planes of the waveguide in Figs. 4(a) and 4(b). One can see that from -0.3 to 0.1 OC in Fig. 4(a), the electric field shifts monotonically with the propagation distance. This is responsible for the poor phase matching of the harmonic emission burst “P” in Fig. 3(a) upon propagation in the waveguide. It also explains the reduction of the cutoff energy at low pressure (5 Torr) shown previously in Fig. 2(a). The ionization and recombination times of the “short”-trajectory electrons for emission bursts “K” and “J” are labeled in Fig. 4(b). First, we can distinguish the phase-matching conditions of the two emission bursts qualitatively. For burst “K,” the electron is ionized around -0.3 OC and is recombined around 0.1 OC. One can see that electric fields between -0.3 and 0.1 OC at different propagation distances are well overlapped, thus leading to favorable phase matching. However, electric fields between 0 and 0.7 OC, corresponding to the time interval of electron ionization and recombination for burst “J,” are greatly shifted in time with the propagation distance. This slippage disfavors phase matching from building up emission bursts as the wave propagates. In addition, the electron excursion time (i.e., the time from ionization to recombination) for burst “K” is much smaller than that for burst “J,” thus, a smaller intrinsic phase is accumulated for burst “K,” causing easily phase matched in the gas medium. Second, more precisely, we can use the above-mentioned ionization and recombination times to carry out quantitative phase-matching analysis in the following. The single-atom phase of the q th-order harmonic is expressed as [63,73,74]

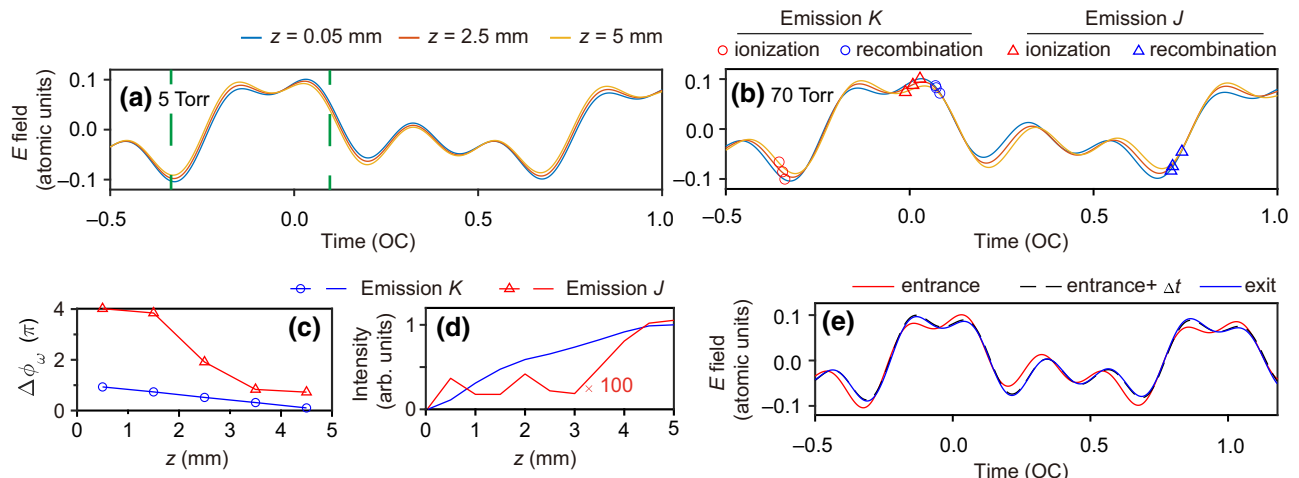


FIG. 4. (a),(b) Electric fields of the three-color waveform at the entrance ($z = 0.05$ mm), the middle ($z = 2.5$ mm), and the exit ($z = 5$ mm) of the hollow waveguide. The radial distance is chosen at $r = 42 \mu\text{m}$. The ionization and recombination times of “short” electron trajectories leading to the 155-eV harmonic are labeled by red and blue marks, respectively. Note that circles and triangles are used to distinguish emission bursts “K” and “J” in Fig. 3, respectively. Phase variation (c) and pulse intensity (d) of the 155-eV harmonic as a function of propagation distance from the two emission bursts. (e) The three-color waveform at the entrance (red solid line) is shifted (black dashed line) according to the values of time shift in Table III, which agrees well with the waveform at the exit (blue solid line). Note that only the analysis in (a) is for 5 Torr, and the others are all for 70 Torr.

$$\Phi_q = q\omega_0 t_r - \int_{t_b}^{t_r} \left[\frac{1}{\hbar} \left(I_p + \frac{p^2}{2m} \right) \right] dt, \quad (13)$$

where q is the harmonic order with respect to the fundamental pulse, ω_0 is the fundamental's angular frequency, I_p is the ionization potential, p is the canonical momentum, and t_b and t_r are the electron ionization and recombination times, respectively. In the moving frame, the change of harmonic phase between two emitters at z and $z + \Delta z$ is $\Delta\Phi_q = \Phi_{q,z} - \Phi_{q,z+\Delta z}$. The phase mismatch is expressed as $\Delta k = \Delta\Phi_q/\Delta z$, and the coherence length is defined by $L_{\text{col}} = \pi/\Delta k$. We calculate $\Delta\Phi_q$ along the 5-mm-long medium with a step of $\Delta z = 1$ mm for harmonic order $q = 201$ (i.e., 155-eV harmonic) in the plateau region, for instance. For two emission bursts, the calculated results are depicted in Fig. 4(c). For burst "K," the phase change is always smaller than π and decreases linearly with the propagation position. In contrast, the phase change of burst "J" varies dramatically from 4π at the beginning to π near the end of the waveguide. The corresponding coherence lengths are listed in Table II. Comparing the coherence lengths of the two emission bursts, it can explain the evolution of their intensities as a function of z in Fig. 4(d), showing that the intensity of "K" burst is building up with propagation while the "J" burst fails to do so.

The IAP generation under the optimal condition has been explained by phase-matched harmonic emission bursts "K." In this gating method, proper three-color waveforms upon propagation in the hollow waveguide are the essential ingredients. We then investigate the shift in time of the three-color laser pulse inside the nonlinear gas medium. For a single-color laser with wavelength λ_x , the variation of the refractive index in the waveguide is [75]

$$\Delta n_x \approx -\frac{\mu_1^2 \lambda_x^2}{8\pi^2 a^2} + p(1-\eta)\delta_1(\lambda_x) - \frac{p\eta N_0 r_e \lambda_x^2}{2\pi}. \quad (14)$$

Here a is waveguide radius, μ_1 is a constant of the waveguide mode, which is 2.405 for the fundamental EH₁₁ mode, η is the ionization probability, and δ_1 , p , N_0 , and r_e are atomic dispersion, gas pressure, neutral atomic density, and classical electron radius, respectively. On the right side of the equation, the first term is due to waveguide mode, the second one is due to atomic dispersion, and the third one is due to plasma effect from the free electrons after ionization. When a laser pulse is propagated from z to $z + \Delta z$,

TABLE II. Coherence lengths of "short"-trajectory harmonics caused by emission bursts "K" and "J," respectively. Harmonic order $q = 201$.

z (mm)	0	1	2	3	4
$L_{\text{col},K}$ (mm)	1.02	1.35	1.93	3.17	9.6
$L_{\text{col},J}$ (mm)	0.24	0.26	0.52	1.20	1.37

its time shift can be written as

$$\begin{aligned} \Delta t &= \Delta n_x \times \Delta z/c \\ &= \Delta t_m + \Delta t_a + \Delta t_p, \end{aligned} \quad (15)$$

where Δt_m , Δt_a , and Δt_p are the time shift due to the waveguide mode, the atomic dispersion, and the plasma, respectively. In Table III, we list values of individual and total time shift accumulated over the 5-mm-long medium for each wavelength component in the three-color waveform. Here positive (negative) value of time shift represents laser pulse moves faster (slower) than the reference frame. These values are quite different for the different wavelength components. For the 0.8-μm laser, $\Delta t = 33$ as has the smallest shift because the positive Δt_a is largely balanced by the negative Δt_m and Δt_p . For the 1.6-μm laser, $\Delta t = -173$ as (absolute value) is bigger since Δt_m caused by the waveguide mode is dominant, and for the 0.4-μm laser, Δt_a due to atomic dispersion is much bigger than the other two terms (comparing their absolute values). How does the time shift for individual wavelength component modify the three-color waveform? To demonstrate it, we plot the electric field of the three-color laser pulse at the entrance (red line) and the exit (blue line) of the hollow waveguide in Fig. 4(e). These waveforms are obtained by numerically solving the MWE of the driving laser. We then shift the electric waveform at the entrance according to the values of time shifts in Table III. The following steps are used: first, the three-color waveform (in time) at the entrance is written in the frequency domain; second, each color component is filtered out to transform back to the time domain to get $E_i(t)$ ($i = 1, 2, 3$) individually; third, $E_i(t)$ is shifted according to Δt for each color. They are then added up coherently to obtain the time-shifted three-color waveform. The resulted waveform (black dashed line), as depicted in Fig. 4(e), overlaps perfectly with the electric field at the exit. Therefore, the change of waveform upon propagation in the waveguide caused by nonlinear effects can be well understood by decomposing the change of refractive index (or time shift) due to each nonlinear term for individual color component.

TABLE III. Time shift (Δt) of each color in three-color laser waveform after propagating 5 mm in the waveguide, which can be decomposed as Δt_m due to waveguide mode dispersion, Δt_a due to neutral atomic dispersion, and Δt_p due to plasma dispersion. Gas pressure is 70 Torr and ionization probability $\eta = 0.15\%$.

Wavelength	Δt_m (as)	Δt_a (as)	Δt_p (as)	Δt (as)
1.6 μm	-200	102	-75	-173
0.8 μm	-50	102	-19	33
0.4 μm	-13	104	-5	86

D. Robustness of IAP generation with respect to phase jitter

In the above gating method for IAP generation, we assume that the phase ϕ_i ($i = 1, 2, 3$) of the three-color optimized waveform in Eq. (12) is precisely defined. However, in real experiments, there are phase jitters between the optical beam channels due to mechanical vibrations of mirrors, air turbulence, or unstabilized CEP. Do they affect the IAP gating method? To check it, we introduce phase jitters in the three-color waveform as

$$E(t) = E_1 A_1(t) \cos(\omega_1 t + \phi_1) + E_2 A_2(t) \cos(\omega_2 t + \phi_2 + \chi_1) + E_3 A_3(t) \cos(\omega_3 t + \phi_3 + \chi_2). \quad (16)$$

Here, χ_1 is the jitter between the 1.6- and 0.8- μm lasers, and χ_2 is the jitter between the 0.8- and 0.4- μm lasers. Other parameters are kept the same as those in Eq. (12). We keep the macroscopic conditions the same as those in Fig. 2, and use the length of waveguide of 5 mm and gas pressure of 70 Torr. We first fix χ_2 and change χ_1 from -0.3π to 0.3π . The resulting attosecond pulses obtained by spectrally filtering high harmonics from 140 to 280 eV are collected in the far field within 1.5 mrad. Their intensity (normalized) profiles are plotted in Fig. 5(a). A clean IAP can be obtained when χ_1 changes from -0.2π to 0.2π , and the pulse energy can be kept above 50% of the optimal one if χ_1 changes from -0.1π to 0.1π as shown in Fig. 5(b). We then fix χ_1 and change χ_2 . The resulting attosecond pulses are shown in Figs. 5(c) and 5(d). One can see that if χ_2 changes from -0.1π to 0.1π , the IAP with considerable pulse energy can still be produced. Thus, for efficient IAP generation, the phase jitter between any two colors should be controlled to within 0.1π . With the development of multicolor laser technology, the required phase jitter of $\pm 0.1\pi$ in our gating method can be realized by splitting the lasers into channels and then adjusting the relative phases by additional optical path in each channel, by controlling the time delay between two colors, or by stabilizing the laser CEP of the fundamental in HHG experiments [16,26,76,77].

In a real experiment, the gas pressure in the waveguide is usually not uniform. We consider a model where the pressure distribution is Lorentzian at the entrance and at the exit, while in between (5 mm long) it is uniform. From the simulation we find (not shown) that at the optimal pressure the macroscopic HHG and IAP are about the same as those in Fig. 2. This is because under the optimal macroscopic pressure the ionization probability is small and phase matching is dominated by the waveguide mode. We point out that it has been found in Major and Varjú [78] that a steep increase of pressure at the beginning of the medium can increase the harmonic flux and decrease the medium length to reach the absorption-limited maximum.

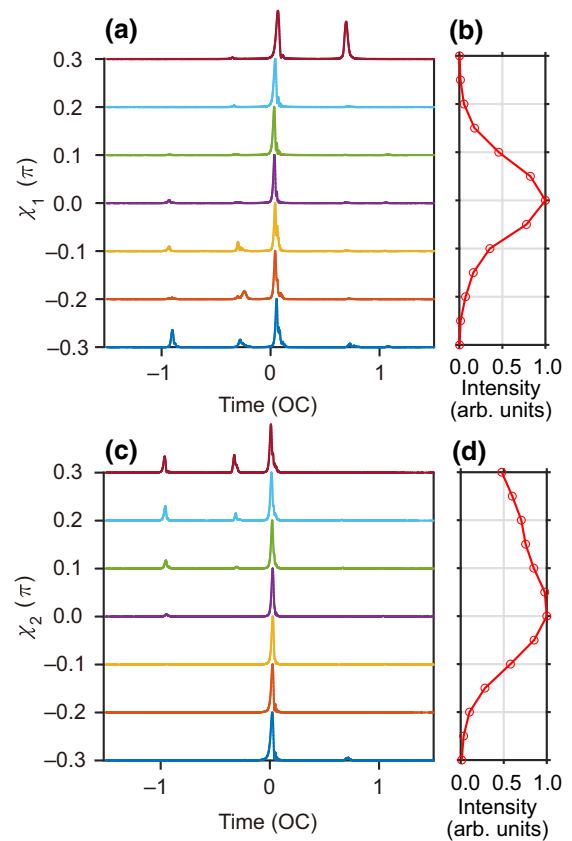


FIG. 5. Attosecond pulses collected in the far field within 1.5 mrad by using high harmonics of three-color waveform from 140 to 280 eV. Intensity (normalized) profiles by varying the phase jitters χ_1 and χ_2 are depicted in (a),(c), respectively, and pulse energies of attosecond pulses are shown in (b),(d).

In their model, atomic dispersion and plasma are assumed to be dominant in the phase matching.

IV. GENERATION OF HHG AND IAP BY THREE-COLOR WAVEFORM IN A GAS CELL

In this section, we examine HHG and IAP generated by the optimized three-color waveform in a gas cell. The length of gas cell is set to be 5 mm, and the waist of the laser beam is 80 μm . The simulated macroscopic HHG spectra are plotted at different gas pressures in Fig. 6(a). The optimal harmonic yields over the extended spectral region are obtained at 70 Torr. In the plateau region, the yield is about one order of magnitude weaker compared to the optimal spectra in the waveguide. Comparing the IAPs synthesized by using the far-field high harmonics within 1.5 mrad, the temporal intensities are displayed in Figs. 6(b) and 6(c), for the pulse generated in the waveguide and in the gas cell, respectively. The former has a FWHM duration of 104 as, while the latter has a FWHM duration of 245 as. To understand these results, we perform time-frequency analysis of high harmonics between 150

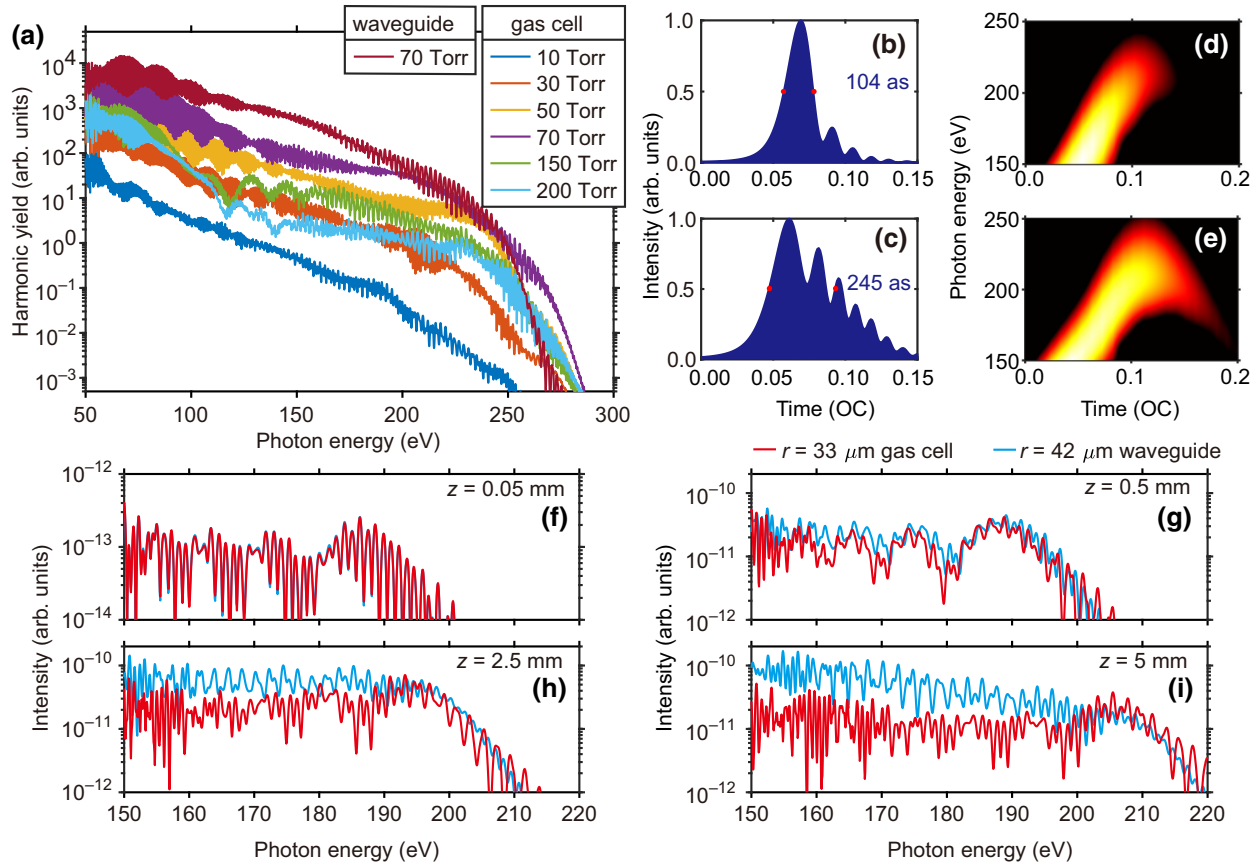


FIG. 6. (a) Simulated HHG spectra by integrating harmonic intensity over the exit plane of the gas cell obtained at different gas pressures. The spectrum obtained in the waveguide at gas pressure of 70 Torr is also shown for comparison. (b),(c) Temporal intensity profiles of isolated attosecond pulse synthesized by high harmonics from 140 to 280 eV in the far field within 1.5 mrad. Time-frequency analysis of the harmonic field at the exit of the waveguide (d) and of the gas cell (e). (f)–(i) Comparison of HHG spectra in the waveguide and in the gas cell at different propagation distances. In (d)–(i), the radial position is chosen at $r = 42 \mu\text{m}$ for the waveguide and at $r = 33 \mu\text{m}$ for the gas cell since initial electric fields are the same at these two positions.

and 250 eV at the exit plane of the medium, at the radial distance of $r = 42 \mu\text{m}$ in the waveguide and $r = 33 \mu\text{m}$ in the gas cell since the initial electric fields are the same, in Figs. 6(d) and 6(e), respectively. In the gas cell, the “long”-trajectory harmonic emissions appear close to the cutoff, and the “short”-trajectory harmonic emissions have larger attochirp compared to the waveguide. Thus, the resulting IAP from the gas cell has a longer duration. We also compare harmonic spectra at different propagation distances in Figs. 6(f)–6(i). At the entrance, the spectra are nearly identical for gas cell and waveguide. With the increase of propagation distance, high harmonics in the waveguide are more efficiently generated. The comparison shows that phase matching in the gas cell and waveguide are quite different.

We can use the same methods in Sec. III to analyze the change of three-color waveform and the phase matching of HHG in the gas cell. The waveforms at the entrance and at the exit of the gas cell at $r = 33 \mu\text{m}$ are plotted in Fig. 7(a). The time shift of each color component after

propagating a distance Δz is

$$\Delta t = \frac{\phi_{\Delta z} \lambda_x}{2\pi c} + \frac{\Delta z}{c} \left(p(1 - \eta) \delta_1(\lambda_x) - \frac{p\eta N_0 r_e \lambda_x^2}{2\pi} \right). \quad (17)$$

In this equation, the first term on the right is the time shift Δt_g due to Gouy phase, which is different from Δt_m due to the dispersion of the waveguide mode in Eq. (14). The Gouy phase $\phi_{\Delta z}$ can be expressed as

$$\phi_{\Delta z} = -\tan^{-1} \left(\frac{2\Delta z}{b} \right) + \left(\frac{r}{w_0} \right)^2 \times \frac{2\Delta z/b}{1 + \left(\frac{2\Delta z}{b} \right)^2}, \quad (18)$$

where b is the confocal parameter and w_0 is the beam waist. The values of time shift are listed in Table IV. The entrance waveform shifted (black dashed line) according to these values are also shown in Fig. 7(a). It does not overlap well with the waveform at the exit, especially at the peak fields.

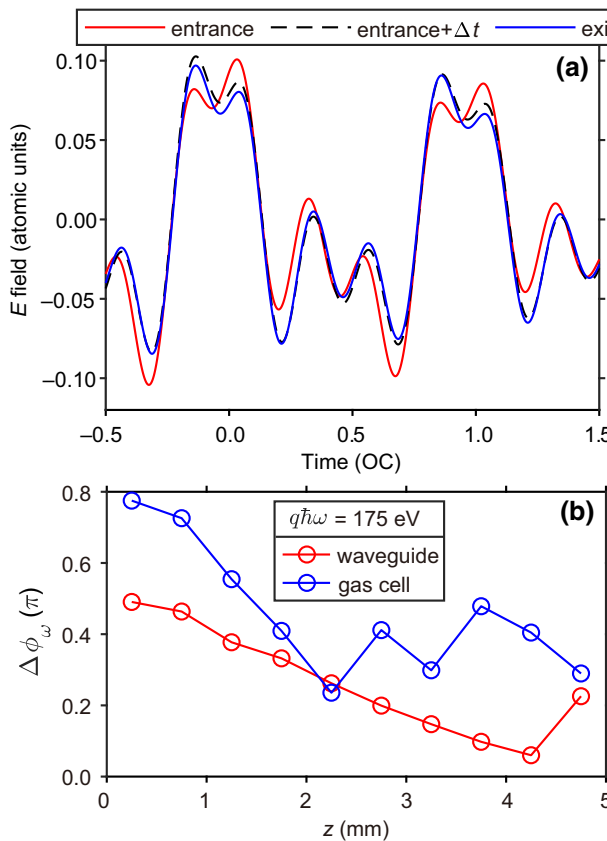


FIG. 7. (a) Electric field of three-color waveform at the entrance (red line) and the exit (blue line) of gas cell and electric field of shifted entrance waveform by a time shift Δt (black dashed line). (b) Comparison of variation of 175-eV harmonic phase over a distance $\Delta z = 0.5$ mm in the gas cell and in the waveguide. Radial positions are the same as those in Fig. 6.

This is because the laser beam diffracts when it propagates in free space, such that the intensity at a fixed radial distance decreases. Thus, adding up individual time shifts caused by a variety of dispersion origins can only partly explain the propagation property of the waveform in the gas cell. This is an obvious difference from propagation in the hollow waveguide.

We can calculate the HHG phase using Eq. (13) in Sec. III C. Take the photon energy of harmonic

TABLE IV. Total time shift (Δt) of each color in three-color waveform by a 5-mm propagation distance in the gas cell, and respective time shifts caused by geometric phase (Δt_g), neutral atomic dispersion (Δt_a), and plasma dispersion (Δt_p) are also given. Assume that gas pressure is 70 Torr and ionization probability is 0.1%.

Wavelength	Δt_g (as)	Δt_a (as)	Δt_p (as)	Δt (as)
1.6 μm	-272	102	-47	-217
0.8 μm	-70	103	-12	21
0.4 μm	-17	104	-3	84

$q\omega\hbar = 175$ eV and set $\Delta z = 0.5$ mm, $\Delta\Phi_q = \Phi_{q,z} - \Phi_{q,z+\Delta z}$ is used to evaluate the degree of phase matching. The variation of HHG phase in a gas cell (at $r = 33 \mu\text{m}$) as a function of z is shown in Fig. 7(b). Although $\Delta\Phi_q$ is always less than π at different propagation distances, it is larger than the values in the waveguide calculated at $r = 42 \mu\text{m}$. This means that under the same initial conditions, phase matching of HHG in the gas cell is worse than that in a waveguide, as discussed in Fig. 7(a). This also explains why harmonic yields in the gas cell are weaker than those in the waveguide, see their propagations in Figs. 6(f)–6(i). These analyses show why isolated attosecond pulses generated by an optimized three-color waveform in a hollow waveguide have much higher flux and shorter duration compared to that in a gas cell.

V. GENERATION OF HHG AND ATTOSECOND PULSES BY OPTIMIZED TWO-COLOR WAVEFORM IN A HOLLOW WAVEGUIDE

Since optimized two-color waveform has also been employed to generate the IAP by synthesizing high harmonics in some narrower spectral regions [69], it is worthwhile to check how it compares to the three-color one for generating IAPs in the SXR region. The two-color waveform consists of 1.6- and 0.8- μm lasers, has the same pulse energy and results in identical ionization level as the three-color one. The parameters of the two-color waveform can be found in Ref. [69]. The comparison of two- and three-color waveforms is demonstrated in Fig. 8(a). The half-cycle periodicity is broken for both waveforms, which is desirable for IAP generation. We use the same waveguide parameters as those in Fig. 3, and simulate the macroscopic HHG spectrum of the two-color waveform under the optimal gas pressure of 70 Torr in Fig. 8(b). Comparing to the spectrum from the three-color waveform, harmonic yields for the two-color one are about 3 orders of magnitude lower from 50 to 100 eV, and one order lower from 140 to 280 eV. This can be explained from Fig. 8(c), in which electric fields at ionization as a function of the kinetic energy of the returning electrons are plotted for “short” and “long” trajectories. The electric field of “short” trajectory for the three-color waveform is much higher than that for the two-color one, while the electric field of “long” trajectory is a bit stronger than that for the “short” one for the two-color waveform. After macroscopic propagation in the hollow waveguide, only “short”-trajectory harmonic emissions can be coherently added up. Finally, we choose high harmonics in a broad spectral region from 140 to 280 eV in the far field within 1.5 mrad to synthesize attosecond pulses. The results are shown in Fig. 8(d). For the two-color waveform, an attosecond pulse train is generated with emission bursts at -0.3 , 0 , and 0.6 OC while an isolated attosecond pulse is generated with a much higher peak field by the three-color waveform. Thus, evidently

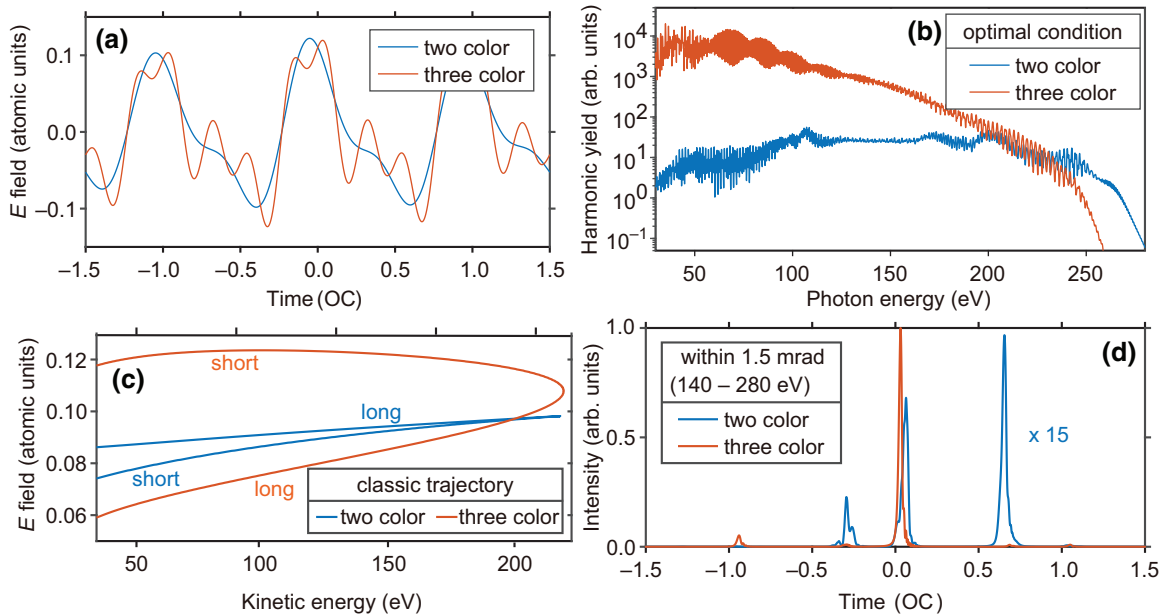


FIG. 8. Comparison of (a) two- and three-color waveforms and (b) resulting macroscopic HHG spectra at optimal condition in the hollow waveguide. (c) Electric field at the ionization versus kinetic energy of returning electron for both “short” and “long” trajectories. (d) Intensity profiles of attosecond pulses by synthesizing high harmonics from 140–280 eV in the far field within 1.5 mrad. Note that results for the two-color waveform are multiplied by a factor of 15 for easy comparison.

the addition of an additional wavelength component of $0.4 \mu\text{m}$, the optimized three-color waveform is capable of significantly enhancing the generation of intense IAP in the SXR region in comparison with the two-color one.

VI. CONCLUSIONS

In summary, we identify an efficient gating method to generate IAPs in the SXR region by using a few-cycle three-color synthesizer in a gas-filled hollow waveguide. We show that, with the pulse energy of 0.62 mJ for input laser beam, the conversion efficiency of SXR high harmonics in the spectral region of 140 to 280 eV can reach 10^{-6} at the optimal gas pressure and waveguide length. By spectrally synthesizing these high harmonics in the far field, an isolated 104-as SXR pulse, with pulse energy of 0.9 nJ and divergence less than 1.5 mrad is obtained without the need to compensate for attochirp. Our simulation is not limited to the specific parameters given in this work. They can be readily scaled up for gaining even higher pulse energy and lower-divergence IAPs according to a macroscopic scaling law [79–81], in which the radius of the waveguide, the beam waist of the input Gaussian laser, and the length of the waveguide are increased while the gas pressure is decreased. For example, with an input pulse energy of 2.48 mJ , one can obtain an isolated SXR pulse with duration of 104 as , energy of 3.6 nJ , and divergence less than 0.75 mrad .

We obtain the great enhancement of shorter duration, higher pulse energy, and lower-divergence IAPs in the

SXR region by optimizing the waveform of a three-color laser and the length and gas pressure in the waveguide. We use time-frequency analysis to illustrate that under such optimal conditions, the harmonic fields achieve optimal phase matching such that the harmonic yields are built up as the harmonics propagate along the waveguide. We further demonstrate that the optimal harmonic yields are rather robust to small variations of the relative phases of the three-color laser beams of ± 0.3 radians. We also show that the enhancement is achieved if the harmonics are generated in a waveguide, but not in a gas cell. In addition, a three-color waveform is needed. If a two-color waveform is used, even if the waveform is optimized, the enhancement of the generated SXR harmonics is much smaller.

Two prerequisites for realizing the exact configuration in our simulations are already available. First, three-color synthesized laser pulses consisting of 1600-nm laser with its second- and third-harmonic fields can be achieved in two ways with current laser technology. One is to efficiently generate the second and third harmonics of a few-cycle fundamental laser collinearly. This has been demonstrated experimentally by Burger *et al.* [49], where the 790-nm laser was used as the fundamental. The other is to generate a coherent broadband supercontinuum with OPA or OPCPA techniques [26,43,46,50], where the spectrum are divided into three channels for accurately controlling the amplitude and phase individually. In the meanwhile, gas-filled hollow waveguide has been commonly employed for HHG [61,82–84], recently developed with

microfluidic glass or ripple patterns [60,85]. Such a setup enables precise control of laser-gas interaction length and gas pressure. Thus, realization of generating high-quality isolated SXR pulses at nanojoule level is expected in the near future. Together with the recent advances in high-power, high-repetition-rate laser [61,86,87], it is possible to further increase the photon flux of SXR IAP by several orders, which would greatly expand its applications in the near future.

ACKNOWLEDGMENTS

This work is supported by the National Natural Science Foundation of China (Grants No. 91950102, No. 11774175, and No. 11834004) and Funding of NJUST (Grant No. TSXK2022D005); C.D.L. is supported by Chemical Science Division, Office of Basic Energy Sciences, Office of Science, US Department of Energy (Grant No. DE-FG02-86ER13491).

- [1] K. Midorikawa, Progress on table-top isolated attosecond light sources, *Nat. Photonics* **16**, 267 (2022).
- [2] F. Calegari, D. Ayuso, A. Trabattoni, L. Belshaw, S. D. Camillis, S. Anumula, F. Frassetto, L. Poletto, A. Palacios, P. Decleva, J. B. Greenwood, F. Martín, and M. Nisoli, Ultrafast electron dynamics in phenylalanine initiated by attosecond pulses, *Science* **346**, 336 (2014).
- [3] N. V. Golubev, J. Vaníček, and A. I. Kuleff, Core-Valence Attosecond Transient Absorption Spectroscopy of Polyatomic Molecules, *Phys. Rev. Lett.* **127**, 123001 (2021).
- [4] L.-Y. Peng, W.-C. Jiang, J.-W. Geng, W.-H. Xiong, and Q. Gong, Tracing and controlling electronic dynamics in atoms and molecules by attosecond pulses, *Phys. Rep.* **575**, 1 (2015).
- [5] Y. Pertot, C. Schmidt, M. Matthews, A. Chauvet, M. Huppert, V. Svoboda, A. von Conta, A. Tehlar, D. Baykusheva, J.-P. Wolf, and H. J. Wörner, Time-resolved x-ray absorption spectroscopy with a water window high-harmonic source, *Science* **355**, 264 (2017).
- [6] M. Hentschel, R. Kienberger, C. Spielmann, G. A. Reidar, N. Milosevic, T. Brabec, P. Corkum, U. Heinzmann, M. Drescher, and F. Krausz, Attosecond metrology, *Nature* **414**, 509 (2001).
- [7] E. Goulielmakis, M. Schultze, M. Hofstetter, V. S. Yakovlev, J. Gagnon, M. Uiberacker, A. L. Aquila, E. M. Gullikson, D. T. Attwood, R. Kienberger, F. Krausz, and U. Kleineberg, Single-cycle nonlinear optics, *Science* **320**, 1614 (2008).
- [8] M.-J. Zhan, P. Ye, H. Teng, X.-K. He, W. Zhang, S.-Y. Zhong, L.-F. Wang, C.-X. Yun, and Z.-Y. Wei, Generation and measurement of isolated 160-attosecond XUV laser pulses at 82 eV, *Chin. Phys. Lett.* **30**, 093201 (2013).
- [9] G. Sansone, E. Benedetti, F. Calegari, C. Vozzi, L. Avaldi, R. Flammini, L. Poletto, P. Villoresi, C. Altucci, R. Velotta, S. Stagira, S. D. Silvestri, and M. Nisoli, Isolated single-cycle attosecond pulses, *Science* **314**, 443 (2006).

- [10] I. J. Sola, E. Mével, L. Elouga, E. Constant, V. Strelkov, L. Poletto, P. Villoresi, E. Benedetti, J.-P. Caumes, S. Stagira, C. Vozzi, G. Sansone, and M. Nisoli, Controlling attosecond electron dynamics by phase-stabilized polarization gating, *Nat. Phys.* **2**, 319 (2006).
- [11] H. Mashiko, S. Gilbertson, C. Li, S. D. Khan, M. M. Shakya, E. Moon, and Z. Chang, Double Optical Gating of High-Order Harmonic Generation with Carrier-Envelope Phase Stabilized Lasers, *Phys. Rev. Lett.* **100**, 103906 (2008).
- [12] K. Zhao, Q. Zhang, M. Chini, Y. Wu, X. Wang, and Z. Chang, Tailoring a 67 attosecond pulse through advantageous phase-mismatch, *Opt. Lett.* **37**, 3891 (2012).
- [13] X. Wang, L. Wang, F. Xiao, D. Zhang, Z. Lü, J. Yuan, and Z. Zhao, Generation of 88 as isolated attosecond pulses with double optical gating, *Chin. Phys. Lett.* **37**, 023201 (2020).
- [14] Z. Yang, W. Cao, X. Chen, J. Zhang, Y. Mo, H. Xu, K. Mi, Q. Zhang, P. Lan, and P. Lu, All-optical frequency-resolved optical gating for isolated attosecond pulse reconstruction, *Opt. Lett.* **45**, 567 (2020).
- [15] X. Wang, P. Xu, J. Li, H. Yuan, Y. Bai, Y. Wang, and W. Zhao, Isolated attosecond pulse with 159 as duration measured by home built attosecond streaking camera, *Chin. J. Lasers* **47**, 0415002 (2020).
- [16] D. Greening, B. Weaver, A. J. Pettipher, D. J. Walke, E. W. Larsen, J. P. Marangos, and J. W. G. Tisch, Generation and measurement of isolated attosecond pulses with enhanced flux using a two colour synthesized laser field, *Opt. Express* **28**, 23329 (2020).
- [17] E. J. Takahashi, P. Lan, O. D. Mücke, Y. Nabekawa, and K. Midorikawa, Attosecond nonlinear optics using gigawatt-scale isolated attosecond pulses, *Nat. Commun.* **4**, 2691 (2013).
- [18] B. Xue, Y. Tamaru, Y. Fu, H. Yuan, P. Lan, O. D. Mücke, A. Suda, K. Midorikawa, and E. J. Takahashi, A custom-tailored multi-TW optical electric field for gigawatt soft-x-ray isolated attosecond pulses, *Ultrafast Sci.* **2021**, 9828026 (2021).
- [19] F. Ferrari, F. Calegari, M. Lucchini, C. Vozzi, S. Stagira, G. Sansone, and M. Nisoli, High-energy isolated attosecond pulses generated by above-saturation few-cycle fields, *Nat. Photonics* **4**, 875 (2010).
- [20] J. Schötz, B. Förög, W. Schweinberger, I. Lontos, H. Masood, A. Kamal, C. Jakubeit, N. Kling, T. Paasch-Colberg, S. Biswas, M. Högnér, I. Pupeza, M. Alharbi, A. Azzeer, and M. Kling, Phase-Matching for Generation of Isolated Attosecond XUV and Soft-X-Ray Pulses with Few-Cycle Drivers, *Phys. Rev. X* **10**, 041011 (2020).
- [21] X. Tang, K. Wang, B. Li, Y. Chen, C. D. Lin, and C. Jin, Optimal generation and isolation of attosecond pulses in an overdriven ionized medium, *Opt. Lett.* **46**, 5137 (2021).
- [22] J. A. Wheeler, A. Borot, S. Monchocé, H. Vincenti, A. Ricci, A. Malvache, R. Lopez-Martens, and F. Quéré, Attosecond lighthouses from plasma mirrors, *Nat. Photonics* **6**, 829 (2012).
- [23] M.-C. Chen, C. Mancuso, C. Hernández-García, F. Dollar, B. Galloway, D. Popmintchev, P.-C. Huang, B. Walker, L. Plaja, A. A. Jaroń-Becker, A. Becker, M. M. Murnane, H. C. Kapteyn, and T. Popmintchev, Generation of bright isolated attosecond soft x-ray pulses driven by multicycle

- midinfrared lasers, *Proc. Natl. Acad. Sci. USA* **111**, E2361 (2014).
- [24] B. Li, K. Wang, X. Tang, Y. Chen, C. D. Lin, and C. Jin, Generation of isolated soft x-ray attosecond pulses with mid-infrared driving lasers via transient phase-matching gating, *New J. Phys.* **23**, 073051 (2021).
- [25] C. Hernández-García, T. Popmintchev, M. M. Murnane, H. C. Kapteyn, L. Plaja, A. Becker, and A. Jaron-Becker, Isolated broadband attosecond pulse generation with near- and mid-infrared driver pulses via time-gated phase matching, *Opt. Express* **25**, 11855 (2017).
- [26] B. Xue, Y. Tamaru, Y. Fu, H. Yuan, P. Lan, O. D. Mücke, A. Suda, K. Midorikawa, and E. J. Takahashi, Fully stabilized multi-TW optical waveform synthesizer: Toward gigawatt isolated attosecond pulses, *Sci. Adv.* **6**, eaay2802 (2020).
- [27] B. Xue, K. Midorikawa, and E. J. Takahashi, Gigawatt-class, tabletop, isolated-attosecond-pulse light source, *Optica* **9**, 360 (2022).
- [28] T. Gaumnitz, A. Jain, Y. Pertot, M. Huppert, I. Jordan, F. Ardana-Lamas, and H. J. Wörner, Streaking of 43-attosecond soft-x-ray pulses generated by a passively CEP-stable mid-infrared driver, *Opt. Express* **25**, 27506 (2017).
- [29] J. Li, X. Ren, Y. Yin, K. Zhao, A. Chew, Y. Cheng, E. Cunningham, Y. Wang, S. Hu, Y. Wu, M. Chini, and Z. Chang, 53-attosecond x-ray pulses reach the carbon K-edge, *Nat. Commun.* **8**, 186 (2017).
- [30] J. Li, A. Chew, S. Hu, J. White, X. Ren, S. Han, Y. Yin, Y. Wang, Y. Wu, and Z. Chang, Double optical gating for generating high flux isolated attosecond pulses in the soft x-ray regime, *Opt. Express* **27**, 30280 (2019).
- [31] S. L. Cousin, N. D. Palo, B. Buades, S. M. Teichmann, M. Reduzzi, M. Devetta, A. Kheifets, G. Sansone, and J. Biegert, Attosecond Streaking in the Water Window: A New Regime of Attosecond Pulse Characterization, *Phys. Rev. X* **7**, 041030 (2017).
- [32] S. M. Teichmann, F. Silva, S. L. Cousin, M. Hemmer, and J. Biegert, 0.5-keV soft x-ray attosecond continua, *Nat. Commun.* **7**, 11493 (2016).
- [33] A. S. Johnson, D. R. Austin, D. A. Wood, C. Brahms, A. Gregory, K. B. Holzner, S. Jarosch, E. W. Larsen, S. Parker, C. S. Strüber, P. Ye, J. W. G. Tisch, and J. P. Marangos, High-flux soft x-ray harmonic generation from ionization-shaped few-cycle laser pulses, *Sci. Adv.* **4**, eaar3761 (2018).
- [34] Y. Fu, K. Nishimura, R. Shao, A. Suda, K. Midorikawa, P. Lan, and E. J. Takahashi, High efficiency ultrafast water-window harmonic generation for single-shot soft x-ray spectroscopy, *Commun. Phys.* **3**, 92 (2020).
- [35] K. Nishimura, Y. Fu, A. Suda, K. Midorikawa, and E. J. Takahashi, Apparatus for generation of nanojoule-class water-window high-order harmonics, *Rev. Sci. Instrum.* **92**, 063001 (2021).
- [36] H. Wikmark, C. Guo, J. Vogelsang, P. W. Smorenburg, H. Coudert-Alteirac, J. Lahl, J. Peschel, P. Rudawski, H. Dacasa, S. Carlström, S. Maclot, M. B. Gaarde, P. Johnsson, C. L. Arnold, and A. L'Huillier, Spatiotemporal coupling of attosecond pulses, *Proc. Natl. Acad. Sci. USA* **116**, 4779 (2019).
- [37] L. Quintard, V. Strelkov, J. Vabek, O. Hort, A. Dubrouil, D. Descamps, F. Burgy, C. Péjot, E. Mével, F. Catoire, and E. Constant, Optics-less focusing of XUV high-order harmonics, *Sci. Adv.* **5**, eaau7175 (2019).
- [38] S. R. Abbing, F. Campi, F. S. Sajadian, N. Lin, P. Smorenburg, and P. M. Kraus, Divergence Control of High-Harmonic Generation, *Phys. Rev. Appl.* **13**, 054029 (2020).
- [39] L. Rego, N. J. Brooks, Q. L. D. Nguyen, J. S. Román, I. Binnie, L. Plaja, H. C. Kapteyn, M. M. Murnane, and C. Hernández-García, Necklace-structured high-harmonic generation for low-divergence, soft x-ray harmonic combs with tunable line spacing, *Sci. Adv.* **8**, eabj7380 (2022).
- [40] E. J. Takahashi, T. Kanai, K. L. Ishikawa, Y. Nabekawa, and K. Midorikawa, Coherent Water Window X Ray by Phase-Matched High-Order Harmonic Generation in Neutral Media, *Phys. Rev. Lett.* **101**, 253901 (2008).
- [41] J. Yao, H. Xiong, H. Xu, Y. Fu, B. Zeng, W. Chu, Y. Cheng, Z. Xu, X. Liu, and J. Chen, A systematic investigation of high harmonic generation using mid-infrared driving laser pulses, *Sci. China Phys. Mech. Astron.* **53**, 1054 (2010).
- [42] L. E. Chipperfield, J. S. Robinson, J. W. G. Tisch, and J. P. Marangos, Ideal Waveform to Generate the Maximum Possible Electron Recollision Energy for Any Given Oscillation Period, *Phys. Rev. Lett.* **102**, 063003 (2009).
- [43] S. Haessler, T. Balčiūnas, G. Fan, G. Andriukaitis, A. Pugžlys, A. Baltuška, T. Witting, R. Squibb, A. Zaïr, J. Tisch, J. Marangos, and L. Chipperfield, Optimization of Quantum Trajectories Driven by Strong-Field Waveforms, *Phys. Rev. X* **4**, 021028 (2014).
- [44] C. Jin and C. D. Lin, Optimization of multi-color laser waveform for high-order harmonic generation, *Chin. Phys. B* **25**, 094213 (2016).
- [45] L. He, G. Yuan, K. Wang, W. Hua, C. Yu, and C. Jin, Optimization of temporal gate by two-color chirped lasers for the generation of isolated attosecond pulse in soft x rays, *Photonics Res.* **7**, 1407 (2019).
- [46] A. Wirth, M. T. Hassan, I. Grguraš, J. Gagnon, A. Moulet, T. T. Luu, S. Pabst, R. Santra, Z. A. Alahmed, A. M. Azzeer, V. S. Yakovlev, V. Pervak, F. Krausz, and E. Goulielmakis, Synthesized light transients, *Science* **334**, 195 (2011).
- [47] S.-W. Huang, G. Cirmi, J. Moses, K.-H. Hong, S. Bhardwaj, J. R. Birge, L.-J. Chen, E. Li, B. J. Eggleton, G. Cerullo, and F. X. Kärtner, High-energy pulse synthesis with sub-cycle waveform control for strong-field physics, *Nat. Photonics* **5**, 475 (2011).
- [48] P. Wei, J. Miao, Z. Zeng, C. Li, X. Ge, R. Li, and Z. Xu, Selective Enhancement of a Single Harmonic Emission in a Driving Laser Field with Subcycle Waveform Control, *Phys. Rev. Lett.* **110**, 233903 (2013).
- [49] C. Burger, W. F. Frisch, T. M. Kardaś, M. Trubetskoy, V. Pervak, R. Moshammer, B. Bergues, M. F. Kling, and P. Wnuk, Compact and flexible harmonic generator and three-color synthesizer for femtosecond coherent control and time-resolved studies, *Opt. Express* **25**, 31130 (2017).
- [50] A. Alismail, H. Wang, G. Barbiero, N. Altwaijry, S. A. Hussain, V. Pervak, W. Schweinberger, A. M. Azzeer, F. Krausz, and H. Fattahi, Multi-octave, CEP-stable source for high-energy field synthesis, *Sci. Adv.* **6**, eaax3408 (2020).
- [51] Y. Yang, R. E. Mainz, G. M. Rossi, F. Scheiba, M. A. Silva-Toledo, P. D. Keathley, G. Cirmi, and F. X. Kärtner, Strong-field coherent control of isolated attosecond pulse generation, *Nat. Commun.* **12**, 6641 (2021).

- [52] C. Jin, G. Wang, H. Wei, A.-T. Le, and C. D. Lin, Waveforms for optimal sub-keV high-order harmonics with synthesized two- or three-colour laser fields, *Nat. Commun.* **5**, 4003 (2014).
- [53] T. Popmintchev, M.-C. Chen, A. Bahabad, M. Gerrity, P. Sidorenko, O. Cohen, I. P. Christov, M. M. Murnane, and H. C. Kapteyn, Phase matching of high harmonic generation in the soft and hard x-ray regions of the spectrum, *Proc. Natl. Acad. Sci. USA* **106**, 10516 (2009).
- [54] E. A. Gibson, A. Paul, N. Wagner, R. Tobey, D. Gaudiosi, S. Backus, I. P. Christov, A. Aquila, E. M. Gullikson, D. T. Attwood, M. M. Murnane, and H. C. Kapteyn, Coherent soft x-ray generation in the water window with quasi-phase matching, *Science* **302**, 95 (2003).
- [55] F. Wiegandt, P. N. Anderson, F. Yu, D. J. Treacher, D. T. Lloyd, P. J. Mosley, S. M. Hooker, and I. A. Walmsley, Quasi-phase-matched high-harmonic generation in gas-filled hollow-core photonic crystal fiber, *Optica* **6**, 442 (2019).
- [56] M. Zepf, B. Dromey, M. Landreman, P. Foster, and S. M. Hooker, Bright Quasi-Phase-Matched Soft-X-Ray Harmonic Radiation from Argon Ions, *Phys. Rev. Lett.* **99**, 143901 (2007).
- [57] X. Zhang, A. L. Lytle, T. Popmintchev, X. Zhou, H. C. Kapteyn, M. M. Murnane, and O. Cohen, Quasi-phase-matching and quantum-path control of high-harmonic generation using counterpropagating light, *Nat. Phys.* **3**, 270 (2007).
- [58] T. Popmintchev, M.-C. Chen, P. Arpin, M. M. Murnane, and H. C. Kapteyn, The attosecond nonlinear optics of bright coherent x-ray generation, *Nat. Photonics* **4**, 822 (2010).
- [59] T. J. Butcher, P. N. Anderson, R. T. Chapman, P. Horak, J. G. Frey, and W. S. Brocklesby, Bright extreme-ultraviolet high-order-harmonic radiation from optimized pulse compression in short hollow waveguides, *Phys. Rev. A* **87**, 043822 (2013).
- [60] A. G. Ciriolo, R. M. Vázquez, V. Tosa, A. Frezzotti, G. Crippa, M. Devetta, D. Faccialá, F. Frassetto, L. Poletto, A. Pusala, C. Vozzi, R. Osellame, and S. Stagira, High-order harmonic generation in a microfluidic glass device, *J. Phys. Photonics* **2**, 024005 (2020).
- [61] M. Gebhardt, T. Heuermann, R. Klas, C. Liu, A. Kirsche, M. Lenski, Z. Wang, C. Gaida, J. E. Antonio-Lopez, A. Schülzgen, R. Amezcua-Correa, J. Rothhardt, and J. Limpert, Bright, high-repetition-rate water window soft x-ray source enabled by nonlinear pulse self-compression in an antiresonant hollow-core fibre, *Light Sci. Appl.* **10**, 36 (2021).
- [62] C. D. Lin, A.-T. Le, C. Jin, and H. Wei, Elements of the quantitative rescattering theory, *J. Phys. B: At. Mol. Opt. Phys.* **51**, 104001 (2018).
- [63] M. Lewenstein, P. Balcou, M. Y. Ivanov, A. L'Huillier, and P. B. Corkum, Theory of high-harmonic generation by low-frequency laser fields, *Phys. Rev. A* **49**, 2117 (1994).
- [64] S.-F. Zhao, Y. Wang, G. Wang, and X.-X. Zhou, Validity of the quantitative rescattering theory for high-order harmonic generation of atoms in two-color laser pulses, *Opt. Commun.* **328**, 30 (2014).
- [65] M. B. Gaarde, J. L. Tate, and K. J. Schafer, Macroscopic aspects of attosecond pulse generation, *J. Phys. B: At. Mol. Opt. Phys.* **41**, 132001 (2008).
- [66] C. Jin, A.-T. Le, C. A. Trallero-Herrero, and C. D. Lin, Generation of isolated attosecond pulses in the far field by spatial filtering with an intense few-cycle mid-infrared laser, *Phys. Rev. A* **84**, 043411 (2011).
- [67] V. Tosa, H. T. Kim, I. J. Kim, and C. H. Nam, High-order harmonic generation by chirped and self-guided femtosecond laser pulses. I. Spatial and spectral analysis, *Phys. Rev. A* **71**, 063808 (2005).
- [68] C. Courtois, A. Couairon, B. Cros, J. R. Marquès, and G. Matthieu, Propagation of intense ultrashort laser pulses in a plasma filled capillary tube: Simulations and experiments, *Phys. Plasmas* **8**, 3445 (2001).
- [69] C. Jin, K.-H. Hong, and C. D. Lin, Optimal generation of spatially coherent soft x-ray isolated attosecond pulses in a gas-filled waveguide using two-color synthesized laser pulses, *Sci. Rep.* **6**, 38165 (2016).
- [70] F. Dorchies, J. R. Marquès, B. Cros, G. Matthieu, C. Courtois, T. Vélikorousov, P. Audebert, J. P. Geindre, S. Rebibo, G. Hamoniaux, and F. Amiranoff, Monomode Guiding of 10^{16}W/cm^2 Laser Pulses over 100 Rayleigh Lengths in Hollow Capillary Dielectric Tubes, *Phys. Rev. Lett.* **82**, 4655 (1999).
- [71] M. B. Gaarde, Time-frequency representations of high order harmonics, *Opt. Express* **8**, 529 (2001).
- [72] X.-M. Tong and S.-I. Chu, Probing the spectral and temporal structures of high-order harmonic generation in intense laser pulses, *Phys. Rev. A* **61**, 021802 (2000).
- [73] P. Balcou, P. Salières, A. L'Huillier, and M. Lewenstein, Generalized phase-matching conditions for high harmonics: The role of field-gradient forces, *Phys. Rev. A* **55**, 3204 (1997).
- [74] H.-W. Sun, P.-C. Huang, Y.-H. Tzeng, J.-T. Huang, C. D. Lin, C. Jin, and M.-C. Chen, Extended phase matching of high harmonic generation by plasma-induced defocusing, *Optica* **4**, 976 (2017).
- [75] C. Jin, G. J. Stein, K.-H. Hong, and C. D. Lin, Generation of Bright, Spatially Coherent Soft X-Ray High Harmonics in a Hollow Waveguide Using Two-Color Synthesized Laser Pulses, *Phys. Rev. Lett.* **115**, 043901 (2015).
- [76] M. Musheghyan, P. P. Geetha, D. Faccialà, A. Pusala, G. Crippa, A. Campolo, A. G. Ciriolo, M. Devetta, A. Assion, C. Manzoni, C. Vozzi, and S. Stagira, Tunable, few-cycle, CEP-stable mid-IR optical parametric amplifier for strong field applications, *J. Phys. B: At. Mol. Opt. Phys.* **53**, 185402 (2020).
- [77] T. Severt, J. Troß, G. Kolliopoulos, I. Ben-Itzhak, and C. A. Trallero-Herrero, Enhancing high-order harmonic generation by controlling the diffusion of the electron wave packet, *Optica* **8**, 1113 (2021).
- [78] B. Major and K. Varjú, Extended model for optimizing high-order harmonic generation in absorbing gases, *J. Phys. B: At. Mol. Opt. Phys.* **54**, 224002 (2021).
- [79] C. M. Heyl, H. Coudert-Alteirac, M. Miranda, M. Louisy, K. Kovacs, V. Tosa, E. Balogh, K. Varjú, A. L'Huillier, A. Couairon, and C. L. Arnold, Scale-invariant nonlinear optics in gases, *Optica* **3**, 75 (2016).
- [80] C. M. Heyl, C. L. Arnold, A. Couairon, and A. L'Huillier, Introduction to macroscopic power scaling principles for high-order harmonic generation, *J. Phys. B: At. Mol. Opt. Phys.* **50**, 013001 (2017).

- [81] C. Jin and C. D. Lin, Control of soft x-ray high harmonic spectrum by using two-color laser pulses, [Photonics Res. **6**, 434 \(2018\)](#).
- [82] K. Cassou, S. Daboussi, O. Hort, O. Guilbaud, D. Descamps, S. Petit, E. Mével, E. Constant, and S. Kazamias, Enhanced high harmonic generation driven by high-intensity laser in argon gas-filled hollow core waveguide, [Opt. Lett. **39**, 3770 \(2014\)](#).
- [83] E. A. Gibson, A. Paul, N. Wagner, R. Tobey, S. Backus, I. P. Christov, M. M. Murnane, and H. C. Kapteyn, High-Order Harmonic Generation up to 250 eV from Highly Ionized Argon, [Phys. Rev. Lett. **92**, 033001 \(2004\)](#).
- [84] T. Popmintchev, M.-C. Chen, D. Popmintchev, P. Arpin, S. Brown, S. Ališauskas, G. Andriukaitis, T. Balčiunas, O. D. Mücke, A. Pugzlys, A. Baltuška, B. Shim, S. E. Schrauth, A. Gaeta, C. Hernández-García, L. Plaja, A. Becker, A. Jaron-Becker, M. M. Murnane, and H. C. Kapteyn, Bright coherent ultrahigh harmonics in the keV x-ray regime from mid-infrared femtosecond lasers, [Science **336**, 1287 \(2012\)](#).
- [85] V. Tosa, A. G. Ciriolo, R. M. Vazquez, C. Vozzi, and S. Stagira, Modeling femtosecond pulse propagation and high harmonics generation in hollow core fibers, [Epj Web Conf. **255**, 11005 \(2021\)](#).
- [86] J. Pupeikis, P.-A. Chevreuil, N. Bigler, L. Gallmann, C. R. Phillips, and U. Keller, Water window soft x-ray source enabled by a 25 W few-cycle 2.2 μm OPCPA at 100 kHz, [Optica **7**, 168 \(2020\)](#).
- [87] T. Saule, S. Heinrich, J. Schötz, N. Lilienfein, M. Högner, O. deVries, M. Plötner, J. Weitenberg, D. Esser, J. Schulte, P. Russbueldt, J. Limpert, M. F. Kling, U. Kleineberg, and I. Pupeza, High-flux ultrafast extreme-ultraviolet photoemission spectroscopy at 18.4 MHz pulse repetition rate, [Nat. Commun. **10**, 458 \(2019\)](#).